Velocity-dependent optical potential for neutron elastic scattering from 1*p*-shell nuclei

I. N. Ghabar and M. I. Jaghoub*
Physics Department, The University of Jordan, P. C. 11942, Amman, Jordan
(Received 25 February 2015; revised manuscript received 6 April 2015; published 15 June 2015)

Background: The conventional optical model is quite successful in describing the nucleon elastic scattering data from medium and heavy nuclei. However, its success in describing the light 1*p*-shell nuclei is somewhat limited. The velocity-dependent optical potential resulted in a significant improvement in describing the elastic angular distributions for light nuclei in the low energy region.
Purpose: To extend the formalism of the velocity-dependent potential to higher energies, and to assess its importance in describing neutron elastic scattering data from light 1*p*-shell nuclei at high energies.
Method: We fit the angular distribution data for neutron elastic scattering from ^{12}C and ^{16}O using (i) the velocity-dependent optical potential and (ii) the conventional optical potential. The results of the two models are then compared. At low energies, we compare our angular distribution fits with the fits of other works that exist in the literature. Furthermore, the total integrated cross sections in addition to the analyzing power are calculated using the velocity-dependent optical potential and compared to the experimental data.
Results: The velocity-dependent potential resulted in significant improvements in describing the angular distributions particularly in the large-angle scattering region and for certain energy ranges. This model is important where the experimental data show structural effects from nuclear surface deformations, which are important in light nuclei. Furthermore, the calculated total elastic cross sections and analyzing power are in good agreement with the experimental data.
Conclusions: The velocity-dependent potential gives rise to surface-peaked real terms in the optical model. Such terms account, at least partly, for the structural effects seen in the angular distribution data. The energy range over which the surface terms are needed is found to depend on the target nucleus. Other works that have introduced real surface terms in the optical potential are discussed.

DOI: 10.1103/PhysRevC.91.064308 PACS number(s): 25.40.Dn, 03.65.Nk, 24.10.Ht

I. INTRODUCTION

The phenomenological optical potential is known to provide an excellent description for the nucleon elastic scattering process from medium and heavy mass nuclei [1]. For example, an extensive study presented local and global optical potentials for neutron and proton elastic scattering from nuclei in the mass range $24 \leqslant A \leqslant 209$ and over the energy interval 1 KeV up to 200 MeV [2]. However, the conventional optical model (COM) has not enjoyed the same degree of success when applied to light nuclei, particularly 1*p*-shell nuclei, that have prominent structural effects. In Ref. [3], the differential cross sections for elastic neutron scattering from the light ^{12}C and the heavy ^{208}Pb were measured at 96 MeV incident energy in the interval 10°–70°. The authors compared their measured angular distributions with phenomenological [2,4,5] and microscopic [6–8] optical model calculations. All the models resulted in good agreements with the ^{208}Pb data. But for the 1*p*-shell ^{12}C nucleus, significant differences were observed between the experimental data and the predictions of the phenomenological and microscopic models particularly in the 30°–50° range. The authors suggested that for the light ^{12}C nucleus, surface effects and deformations in addition to diffuseness of the nuclear edge may be responsible for the disagreement between the theoretical models and the experimental data.

An older work [9] analyzed neutron and proton elastic scattering data from 1*p*-shell nuclei over the 9- to 15-MeV energy range covering the angular 25°–160° interval. Energy-dependent parameter sets were obtained for individual nuclei that reasonably described the experimental elastic angular distributions particularly where resonance structure was not prominent. The authors concluded that the optical model fits corresponding to nucleon scattering from light nuclei were not as good as those for the heavy ones, which show less surface deformations and structural effects. Proton elastic scattering from 1*p*-shell nuclei was also considered in Ref. [10] over the interval 10–50 MeV. For the case of proton scattering from ^{12}C, the optical model fits corresponding to incident neutron energies above 19 MeV reproduced the overall features of the angular distribution data. Below 19 MeV, however, the optical model calculations for the angular distributions resulted in two minima while only one was experimentally observed, and the calculated angular distributions were generally below the corresponding experimental data. One important observation is that for ^{12}C, ^{14}N, and ^{16}O, the positions of the large angle minima in the angular distributions were not correctly reproduced. Such minima are usually associated with the presence of nonlocalities that are partly from coupling of the ground state of the target nucleus to inelastic excitations [11]. In fact, it was pointed out that at low incident energies the nucleon elastic scattering from ^{16}O shows a minimum around 120°, that could not be fitted with phenomenological or microscopic local optical potentials [11].

*mjaghoub@ju.edu.jo

In a recent work [12] neutron elastic scattering from the light ^{12}C nucleus was considered over the energy interval 10–20 MeV using a nonlocal velocity-dependent optical potential (VDP). This model resulted in excellent fits to the elastic angular distribution data over the full angular range, particularly the large-angle minima. Although the polarization data were not used in the search for the fit parameters, the analyzing power calculations using the VDP resulted in good agreement with the experimental data. As we shall see in the next section, the Schrödinger equation for a VDP contains terms that are proportional to the derivative of a Woods-Saxon potential. Using the same model, neutron scattering from the heavier ^{40}Ca was studied in the energy range 10–20 MeV [13], while proton elastic scattering from ^{12}C, ^{16}O, ^{40}Ca, and ^{58}Ni was investigated in the 10- to 40-MeV range [14]. In the latter two works, the calculated VDP elastic angular distributions agreed well with the corresponding experimental data even in the large angle scattering region, where the conventional optical model (COM) does not usually lead to good fits.

In this work, we shall investigate the importance of the VDP at higher energies corresponding to neutron elastic scattering from the ^{12}C and ^{16}O $1p$-shell nuclei. We shall start by expressing the Schrödinger equation for a VDP in the standard form, which leads to a local but energy-dependent potential with real surface terms that are proportional to the derivatives of the nuclear matter density. This is important for light nuclei which have diffused edges and deformed surfaces. Other formalisms also lead to optical potentials containing a real surface term. For example, Mau started from the smooth Hartree-Fock (HF) potential, for the valence neutron in the mean field of the nuclear core, and calculated the correction to this HF potential resulting from the coupling of single-particle states to the random phase approximation collective one-phonon states of the core [15]. This coupling was found to be responsible for the inversion of the sequence $1/2^-$ and $1/2^+$ states in the one-neutron halo ^{11}Be nucleus [15]. Furthermore, coupling of single-particle states to collective excitations of the nuclear core in $1p$-shell nuclei was considered in [18] and resulted in a real surface term correction to the smooth HF potential, thus explaining the ground states of ^{11}Li, ^{12}Be, and ^{14}C nuclei which are not possible to describe using usual models suitable for more 'normal" many-body systems. Furthermore, the dispersive optical model (DOM) formalism results in a surface peaked real term as a direct consequence of the dispersive relation that connects the real part of the optical potential to the imaginary one, which has a surface term component [16]. A recent work [17] fitted the elastic angular distributions for neutron scattering from the light ^{9}Be, which is known for its anomalously large deformation and surface effects [19], using two potentials. One is a dispersive optical potential. The other is a conventional optical potential with a real surface peaked term similar to that suggested in [18]. The authors argued that in both cases the surface term simulated the effects of coupling to surface degrees of freedom. However, as reported in [17], it is important to note that the COM with a surface term has resulted in better angular distribution fits for the $n-{}^{9}$Be elastic scattering process than the DOM model.

The real surface term obtained by considering coupling of single-particle states to collective core excitations or through the dispersive relation is essentially a correction to the mean field HF smooth potential, and accounts for the fact that the target nucleus may not remain in the ground state during the elastic scattering process [20]. One difference between the aforementioned formalisms and the VDP formalism is that the later results in three real surface terms which are proportional to the first and higher order derivatives of the nuclear matter density, which might better describe the effects of surface deformations in light nuclei. This might explain the excellent elastic angular distribution fits for nucleon scattering from the light $1p$-shell nuclei in Refs. [12] and [14].

II. THE NONLOCAL VELOCITY-DEPENDENT OPTICAL POTENTIAL

The velocity-dependent potential (VDP) was first introduced in [21] to explain the predominantly p-wave nature of the pion-nucleon scattering. It may be expressed in the form,

$$\begin{aligned}\hat{V}(r,p) &= V(r)+\frac{\hbar^2}{2\mu}\nabla\cdot\rho(r)\nabla,\\ &= V(r)+\frac{\hbar^2}{2\mu}[\rho(r)\nabla^2+\nabla\rho(r)\cdot\nabla],\end{aligned}\tag{1}$$

where μ is the nucleon-nucleus reduced mass and $\rho(r)$ is a smooth function of the radial variable r. The last gradient term that acts on the wave function can be interpreted as the first term of a Taylor series expansion that displaces the wave function from point $\mathbf{r}$ to a different location $\mathbf{r}'$. Therefore, the velocity-dependent potential $\hat{V}(r,p)$ plays the role of a nonlocal potential $V(\mathbf{r},\mathbf{r}')$ [22]. In Eq. (1) the conventional optical potential $V(r)$ is given by

$$\begin{aligned}V(r) =& -V_0 f(r,x_0)+4ia_w W_d\frac{d}{dr}f(r,x_w)\\ &+\frac{2}{r}\left(\frac{\hbar}{m_\pi c}\right)^2(V_{\rm so}+iW_{\rm so})\frac{d}{dr}f(r,x_{\rm so})\vec{\sigma}\cdot\vec{I},\end{aligned}\tag{2}$$

where m_π is the pion mass. This is different from all the works in Refs. [12–14] in which the reduced mass of the nucleon-nucleus system was used in the spin-orbit term. We have used the pion mass for ease of comparison with the conventional optical model (COM). Furthermore, x_j denotes (r_j,a_j) and so on for the rest of the terms. The function $f(r,x_j)$ has the Woods-Saxon form, namely,

$$f(r,r_j,a_j)=\frac{1}{1+\exp[(r-r_jA^{1/3})/a_j]},\tag{3}$$

with A being the mass number of the target nucleus. As we shall see in Sec. IV, for incident energies around 30 MeV an additional volume term,

$$W_v(r)=W_v f(r,x_0),\tag{4}$$

was needed in $V(r)$ to fit the experimental angular distributions. The function $\rho(r)$ is defined as the first derivative of a Woods-Saxon potential, namely,

$$\rho(r)=\rho_0\,a_\rho\frac{d}{dr}f(r,x_\rho),\tag{5}$$

and hence is proportional to the nuclear matter density. Its effect is expected to be most important in light nuclei that mainly consist of diffused edges and deformed surfaces.

For the above VDP, the corresponding Schrödinger equation takes the form,

$$(1-\rho)v''(r) - \left[v'(r) - \frac{v(r)}{r}\right]\rho' - (1-\rho)\frac{l(l+1)}{r^2}v(r) = \frac{2m}{\hbar^2}[V(r)-E]v(r), \quad (6)$$

where the dependencies of the reduced wave function on k and $\rho(r)$ on r have been suppressed for clarity of presentation. This form was used to determine the effects of small perturbations in the velocity-dependent potential on the bound-state energies [23] and the scattering phase shifts [24].

The last equation can be transformed into the standard form of the Schrödinger equation for an equivalent local but energy-dependent potential $U(r,E)$, through the transformation of Krell and Ericson [25], namely,

$$v(k,r) = \frac{\psi(k,r)}{\sqrt{1-\rho(r)}}, \quad (7)$$

that leads to the following standard Schrödinger equation,

$$\psi''(r) + \left[\frac{2\mu}{\hbar^2}E - \frac{l(l+1)}{r^2} + U(r,E)\right]\psi(r) = 0, \quad (8)$$

where

$$U(r,E) = \frac{1}{(1-\rho)}\left[\frac{\rho''}{2} + \frac{\rho'^2}{4(1-\rho)} + \frac{\rho'}{r} - \frac{2\mu}{\hbar^2}V(r) + \frac{2\mu}{\hbar^2}\rho E\right]. \quad (9)$$

Clearly, the above Schrödinger equation contains terms that are proportional to the first and higher order derivatives of the Woods-Saxon potential, namely $\rho(r)$, $\rho'(r)$, and $\rho''(r)$. In fact, the term $(\rho'(r))^2$ has the same radial form as the real surface term in Eq. (28) of Ref. [18].

In addition to the real surface terms, the energy-dependent potential $U(r,E)$ contains imaginary surface terms as given by the definition of $V(r)$ in Eq. (2), where the second term on the right-hand side is the well-known surface imaginary absorptive term. This term is responsible for all the nonelastic processes that lead to the removal of particle flux from the elastic channel. As already mentioned in the introduction, this term results in a real surface term through the dispersive relation within the framework of the dispersive optical potential. In addition, as we shall see in Sec. IV, at incident neutron energies greater than about 30 MeV, a volume imaginary term is needed to obtain the angular distribution fits. This indicates that for such energies the incident neutron interactions take place inside the nucleus and not just at the surface.

III. FITTING PROCEDURE

The issue of how to judge the *goodness* of an optical potential fit to experimental data was discussed at length in the extensive work of Koning and Delaroche [2]. They argued that the determination of a successful optical potential parameter set is considered successful provided the following three conditions are satisfied: (i) physically meaningful parameters, (ii) the parameters must satisfy a numerical optimization procedure which is usually a minimal value of χ^2, and (iii) a good visual fit. One may also compare the theoretical predictions of integrated cross sections with the experimental values. Because we obtain the VDP parameters by fitting elastic angular distributions we shall see that the theoretical predictions for the total elastic cross section agree better with experimental data than the case for the total reaction cross section. This is true for the VDP, COM, and the potential of Dave and Gould in Ref. [9]. In obtaining our fits we always paid special attention to the quality of the fits at large angles, where structural effects are expected to be important. Although a χ^2 analysis gives an overall indication of the quality of a given fit, we found that a minimal value of χ^2 does not necessarily lead to a best fit to the data in the backward-scattering region. In fact, Perey discussed the issue of optimizing the phenomenological optical potential fits in nuclear scattering and concluded that the value of χ^2 may have little meaning as an estimator of the goodness-of-fit [26]. In this work we always aimed to satisfy all the three conditions listed above. However, if a good visual fit in the large-angle region led to a small increase in the value of χ^2, we chose the fit that best describes the data at large angles. One slight complication with the χ^2 analysis in this work arose from the fact that the Evaluated Nuclear Data File (ENDF), which is the source of the experimental angular distribution data used here, does not list experimental data errors. However, to still use the χ^2 analysis as one of the indicators for the quality of our fits, we assumed a 10% error on each data point, which corresponds to the mean value of the error in the experimental data [27]. We varied the potential parameters until a satisfactory visual fit was obtained in addition to obtaining a minimal value for χ^2 according to the formula,

$$\chi^2 = \frac{1}{N}\sum_{i=0}^{N}\left(\frac{\left(\frac{d\sigma(\theta_i)}{d\Omega}\right)_{\text{theo}} - \left(\frac{d\sigma(\theta_i)}{d\Omega}\right)_{\text{exp}}}{\Delta\left(\frac{d\sigma(\theta_i)}{d\Omega}\right)}\right)^2, \quad (10)$$

$(d\sigma(\theta_i)/d\Omega)_{\text{theo}}$ and $(d\sigma(\theta_i)/d\Omega)_{\text{exp}}$ being the theoretical and experimental differential cross sections, respectively. A smooth variation in addition to a physical meaning of the values of the potential parameters were always of our primary concern. It is known that more than one set of phenomenological optical potential parameters may result in the same fit to the angular distribution data. One example is that different values of the real potential depth V_0 and the diffuseness parameter a_0 leading to the same value of their product $V_0 a_0^2$ result in the same fit. To reduce the effect of this and other ambiguities, the sets of best fit parameters were used to theoretically calculate the analyzing power $A_y(\theta)$ whenever data were available. We then chose the set of parameters that resulted in the best prediction for the experimental analyzing power.

In searching for the fit parameters, the strengths of the real and imaginary central potentials were important to generate the overall behavior of the angular distributions. The *fine tuning* to reproduce the large-angle minima was then achieved by varying the parameters of the real surface and spin-orbit

terms. In particular, the values of ρ_0, r_ρ, and a_ρ associated with surface terms in Eq. (1) were observed to strongly affect the differential cross section values in the backward-scattering region, thus leading to a good fit corresponding to large angles.

IV. RESULTS AND DISCUSSION

As a test of the VDP we shall compare our angular distribution fits to the results of the COM model that exist in the literature in the low energy range. At higher energies, however, we shall fit the experimental data twice, the first by using the VDP, while in the second we use the COM model. By comparing the fits of both models, we shall investigate the importance of the VDP as a function of incident energy. We shall also calculate the total elastic and total reaction cross sections in addition to the analyzing power using the VDP. The theoretically determined values shall be compared to experimental data.

A. The low-energy case

Dave and Gould [9] analyzed neutron elastic angular scattering data from the light ^{6}Li to ^{16}O $1p$-shell nuclei and over the low 7- to 15-MeV energy range. They fixed the geometric parameters for each nucleus but allowed the potential depths to vary with energy. In this work, we compare our angular distribution fits for neutron elastic scattering from ^{12}C to their fits, which they obtained using the COM potential given in Eq. (2). For a meaningful comparison, we have fixed the geometry parameters but allowed a slight variation in the potential depths and ρ_0 as can be seen in Table I. The values of r_ρ and a_ρ were constant at all energies apart from the 15-MeV case, where our fit at large angles could not be obtained without modifying their values. The corresponding angular distribution fits are displayed in Fig. 1. Clearly, the VDP has improved the fits in the large-angle region ($\theta_{\rm cm} > 100^0$) corresponding to the 12.8-, 14-, and 15-MeV incident energies. This region is usually associated with nonlocalities [11] part of which is from coupling of inelastic channels to the ground state of the target nucleus. Evidently, the VDP has three more fit parameters than the COM, but those extra degrees of freedom are only needed when the differential cross sections start to show deep minima in the large-angle scattering region. This is supported by the observation that both the VDP and COM resulted in similar angular distribution fits corresponding to the 9.6-MeV energy, where no prominent minimum in the back-angle region exists. We shall come to the same conclusion in the next section when we extend the VDP to higher energies. It remains to note that, for all the energies considered, the VDP has resulted in better overall fits to the elastic angular distribution data as can be

TABLE I. Velocity-dependent potential best fit parameters for $n - {}^{12}$C elastic angular distributions. The potential depths are in units of MeV, the geometric parameters are in units of Fermi, and ρ_0 is dimensionless. The χ^2 values corresponding to the VDP and DG potentials are also shown.

VDP	$E_{\rm lab}$ (MeV)				
parameters	9.6	11.0	12.8	14.0	15.0
V_0	53.40	52.13	51.98	51.50	49.90
r_0	1.20	1.20	1.20	1.20	1.20
a_0	0.35	0.35	0.35	0.35	0.35
W_d	13.05	13.10	13.18	13.50	13.80
r_w	1.387	1.387	1.387	1.387	1.387
a_w	0.163	0.163	0.163	0.163	0.163
ρ_0	−0.55	−0.10	−0.39	−0.15	−0.99
r_ρ	0.60	0.60	0.60	0.60	1.90
a_ρ	0.35	0.35	0.35	0.35	0.42
$V_{\rm sor}$	5.50	5.50	6.00	5.35	4.40
$V_{\rm soi}$	1.00	1.10	2.60	2.30	1.32
$r_{\rm so}$	1.15	1.15	1.15	1.15	1.15
$a_{\rm so}$	0.5	0.5	0.5	0.5	0.5
χ^2(VDP)	0.8	1.8	2.6	2.0	1.7
χ^2(DG)	2.9	6.4	9.0	3.4	4.5

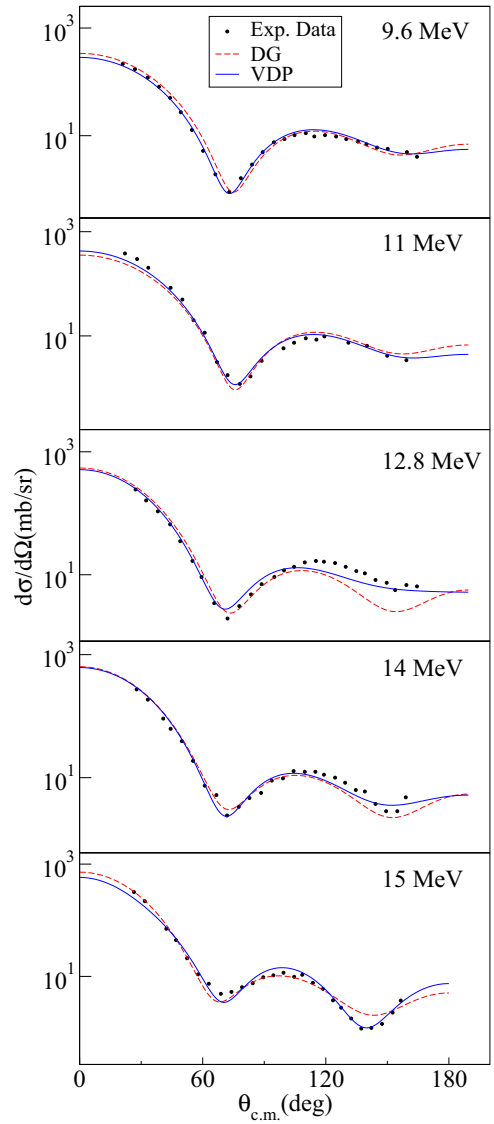

FIG. 1. (Color online) Angular distribution fits for the $n - {}^{12}$C elastic scattering process using the velocity-dependent potential (VDP) and the Dave and Gould (DG) models. The experimental data are obtained from Ref. [28].

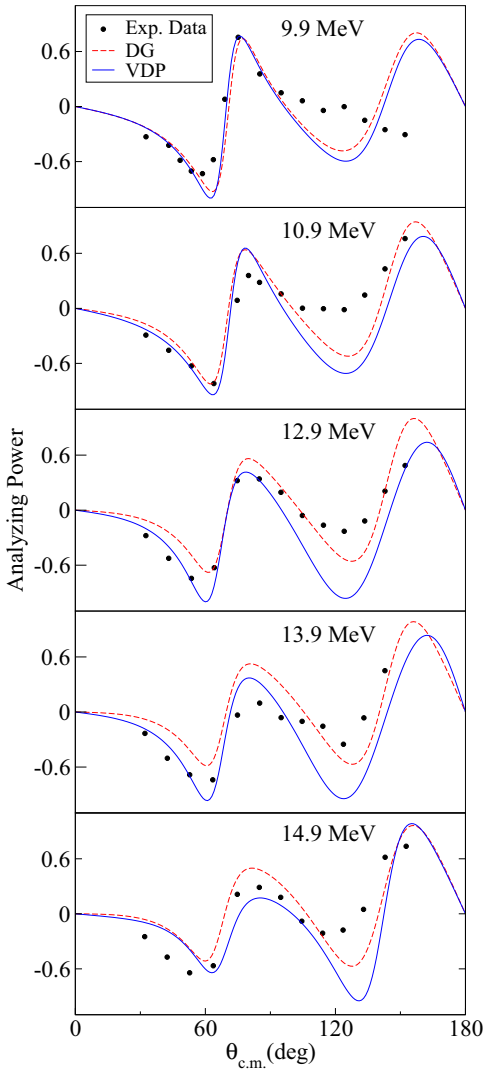

FIG. 2. (Color online) Analyzing power fits for the $n - {}^{12}$C elastic scattering process using the velocity-dependent potential (VDP) and the Dave and Gould (DG) models. The experimental data are obtained from Ref. [28].

seen by inspecting the χ^2 values in Table I. It is worth noting that amongst the strengths of the VDP parts, the strength W_d of the imaginary part shows the least variation with energy. This could be a reflection of the real surface terms accounting, at least partly, for the coupling of the target's ground state to inelastic excitations.

We have also used the VDP and COM formalisms to calculate the analyzing power $A_y(\theta)$. The results are displayed in Fig. 2. Clearly, at small angles both models resulted in reasonable fits to the polarization data, with the VDP calculations being more accurate than the COM results at the 12.9 and 13.9 MeV. At large angles, however, the agreement of both models with experiment is less accurate, with the COM calculations being closer to the experimental data. It is worth noting that the fit to the polarization data could be improved using either model, but that would be at the expense of the quality of the fit to the differential cross sections.

B. Extending the VDP formalism to higher energies

In this section we shall investigate the importance of the VDP at higher energies. We shall consider the cases of elastic neutron scattering from the light $1p$-shell ^{12}C and ^{16}O nuclei over the energy range 12 up to 90 MeV. In each case, we fit the elastic angular distributions using the VDP and the COM formalisms. Wherever experimental polarization data existed, we shall compare the analyzing power calculations of both models with the experimental data.

1. $n - {}^{12}$C elastic scattering

As pointed out in the introduction, several conventional optical and microscopic potentials resulted in significant differences between the calculated theoretical angular distributions and the elastic angular distribution data for the $n - {}^{12}$C scattering process [3]. This was proposed to be a consequence of the surface deformations and diffuseness of the light ^{12}C nucleus. Surface deformations are important as they allow coupling of the target's ground state to inelastic excitation channels, thus modifying the experimental elastic angular distribution data. In fact, coupled channel analyses of inelastic angular distributions of proton scattering from ^{12}C revealed resonance effects in the angular distributions [29]. Such effects are responsible for the enhancement and diminishment of the angular distributions at specific angles particularly in the backward-scattering region [30]. In what follows we shall test the ability of the VDP, which contains real surface-peaked terms, to account for such surface effects.

In this work we have allowed all the potential parameters of the VDP and COM to be energy dependent but kept that dependence down to a minimum. Fixing the geometrical parameters leads to less quality fits compared to those displayed in Figs. 3 and 4. Clearly, the VDP has resulted in excellent fits to the differential cross sections particularly the back-angle scattering regions. The quality of the corresponding fits obtained using the COM model around $\theta_{\rm cm} \approx 120^0$ are less accurate especially over the 17- to 20-MeV range. However, Fig. 4 shows that for incident energies greater than 20 MeV, no deep back-angle minima are present and the COM resulted in excellent fits to the experimental data for the full angular range. The VDP and COM fits are almost identical. At those energies there are no structural effects and hence the need for the surface terms of the VDP no longer exists. We suggest that $\rho(r)$ and its derivatives account, at least partly, for the effects of surface deformations which are responsible for the deep minima in the large-angle scattering region corresponding to incident energies up to 20 MeV.

The best fit parameters for the VDP and COM are given in Tables II and III, respectively. For the VDP and COM models, the values of the potential strengths and geometric parameters show comparable variations with energy. An exception is the behavior of the imaginary surface absorption term, where the parameters W_d, r_w, and a_w belonging to the VDP are more stable than the corresponding values of the COM potential. Furthermore, in comparison to the COM potential, the values of the potential strength W_d corresponding to the VDP are reduced. Because the imaginary surface term accounts for absorption, a reduced W_d value may be seen as an evidence that

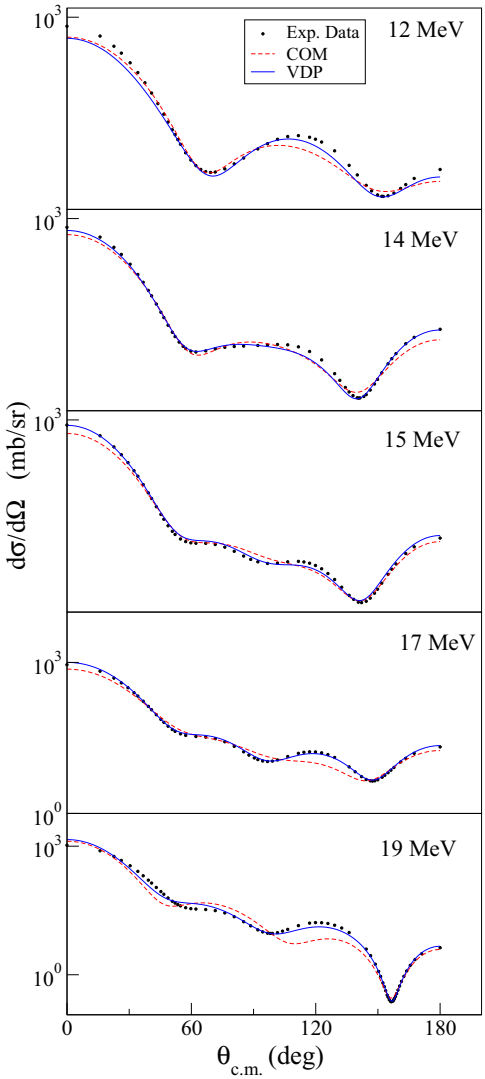

FIG. 3. (Color online) Angular distribution fits for the $n - {}^{12}$C elastic scattering process using the velocity-dependent potential (VDP) and the conventional optical model (COM). The experimental data are obtained from Ref. [31].

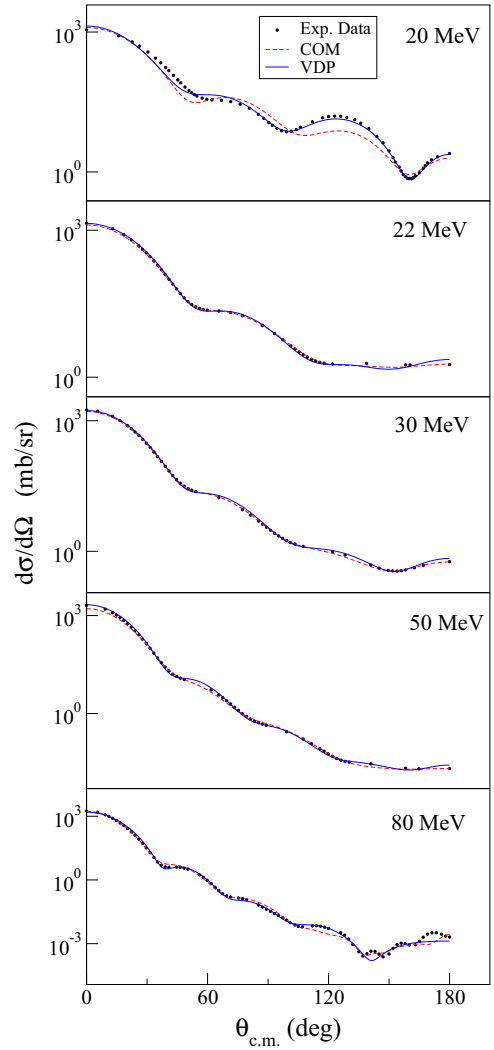

FIG. 4. (Color online) Angular distribution fits for the $n - {}^{12}$C elastic scattering process using the velocity-dependent potential (VDP) and the conventional optical model (COM). The experimental data are obtained from Ref. [31].

the real surface terms simulate coupling to inelastic excitation channels. Inspection of Table III shows that an additional volume term defined by Eq. (4) is needed to achieve the COM fits starting from the 30-MeV incident energy. In this energy range, the interactions of the incident neutron are not limited to the surface region but also take place inside the nuclear volume. During our search for the best fit parameters, we noticed that the parameters of the real surface term $\rho(r)$ have a significant influence on the quality of the fits in the back-angle scattering region. For example, setting $\rho_0 = 0$ at $E_{\rm lab} = 19$ MeV significantly reduces the quality of the fit at large angles. It remains to note that the χ^2 values corresponding to the VDP formalism are clearly smaller than the corresponding ones obtained for the COM potential.

Finally, as shown in Fig. 5, we compare the calculated analyzing powers using the VDP and COM. The two models result in reasonable similar agreements with the experimental data. However, at 13.9 MeV the VDP clearly improves the agreement with the data in the low angle region. At 11.9 MeV, however, the calculated analyzing power using the COM potential is better than that of the VDP at large angles.

2. $n - {}^{16}$O *elastic scattering*

Inspection of the $n - {}^{16}$O elastic angular distribution fits shown in Figs. 6–8 reveals two main differences with the $n - {}^{12}$C elastic scattering case. First, there is a significant deviation between the experimental data and the fits of the COM potential at the position of the first minimum in the 50°–70° angular range. This is most obvious for the 14- to 22-MeV incident energies. The corresponding VDP fits are significantly more accurate. At the lowest 12-MeV incident energy the discrepancy is shifted to a slightly higher angular range with the VDP fit better than that of the COM but does not quite agree with the experimental data. Furthermore, in the back-angle scattering region, the VDP fits

TABLE II. Velocity-dependent potential best fit parameters for $n - {}^{12}$C elastic scattering. Potential depths are in units of MeV, geometric parameters in units of Fermi, and ρ_0 is dimensionless.

VDP	$E_{\rm lab}$(MeV)									
parameters	12	14	15	17	19	20	22	30	50	80
V_0	48.8	49.0	46.5	42.8	41.0	43.3	44.8	44.4	43.8	36.1
r_0	1.196	1.264	1.200	1.136	1.176	1.14	1.216	1.216	1.184	1.147
a_0	0.499	0.471	0.567	0.643	0.893	0.804	0.645	0.629	0.637	0.576
W_v	0.0	0.0	0.0	0.0	0.0	0.0	0.0	0.0	2.4	11.05
W_d	5.7	5.5	4.5	5.4	6.9	5.4	6.5	6.5	6.8	4.0
r_w	1.233	1.130	1.200	1.160	1.381	1.280	1.232	1.232	1.240	1.336
a_w	0.493	0.584	0.596	0.544	0.447	0.560	0.632	0.640	0.640	0.480
ρ_0	−2.356	−0.692	−1.283	−1.812	−2.301	−2.220	0	0	0	0
r_ρ	1.841	1.585	1.451	1.337	1.239	1.181	1.054	1.054	1.054	1.239
a_ρ	0.169	0.216	0.235	0.264	0.163	0.150	0.152	0.152	0.152	0.163
$V_{\rm sor}$	4.8	4.7	4.9	4.4	6.1	4.0	6.0	5.1	4.6	3.4
$V_{\rm soi}$	1.7	0.2	0.1	0.0	1.0	1.1	0.1	0.2	0.1	0.7
$r_{\rm so}$	1.197	0.921	0.896	0.896	0.761	0.971	1.058	1.067	1.059	1.029
$a_{\rm so}$	0.418	0.232	0.269	0.330	0.484	0.315	0.478	0.487	0.497	0.527
χ^2	1.0	0.2	0.4	0.2	2.0	1.8	0.5	0.3	0.8	5.8

are accurate showing a significant improvement over those of the corresponding COM ones particularly at the 17- and 30-MeV incident energies. Second, as can be seen in Figs. 7 and 8, the COM model led to excellent fits to the angular distributions across the full angular range for incident energies greater than 30 MeV. This is unlike the ^{12}C case, where the COM resulted in excellent fits for all angles corresponding to energies greater than 20 MeV. The change of the energy range over which the VDP is needed may be traced to differences in the nuclear structures of the ^{12}C and ^{16}O nuclei. In Fig. 9, we display the analyzing powers calculated using both models. Clearly, both models result in reasonable agreement with the data, with those calculated using the VDP being more accurate especially at the 14-MeV energy. Once again, the fit to the polarization data from either model could be improved, but at the expense of the quality of the angular distribution fits.

The fit parameters for the VDP and COM models are shown in Tables IV–VII, respectively. The common parameters between the two models show similar energy dependence. However, the values of W_d of the VDP model are smaller than those for the COM as was observed in the ^{12}C case. The decrease in the strength of the imaginary absorption term, which accounts for inelastic channels, could be from the real surface terms contributing in accounting for the inelastic excitations that couple to the ground state of the target nucleus. Finally, apart from the case of 27-MeV incident energy, the χ^2 values for the VDP are lower than the corresponding ones for the COM potential.

C. Total cross sections

To test the applicability of the VDP further, we have calculated the total elastic ($\sigma_{\rm tot}^{\rm el}$) and total reaction ($\sigma_{\rm tot}^{r}$) cross sections using the DG, VDP, and COM models. The calculated quantities together with the corresponding experimental values are shown in Tables VIII and X. Inspection of Table VIII shows that both the DG and VDP models have resulted in very good

TABLE III. Conventional optical model best fit parameters for $n - {}^{12}$C elastic scattering. Potential depths are in units of MeV, geometric parameters in units of Fermi, and ρ_0 is dimensionless.

COM	$E_{\rm lab}$(MeV)									
parameters	12	14	15	17	19	20	22	30	50	80
V_0	51.99	51.00	49.99	51.50	51.01	50.00	49.87	47.07	35.00	26.99
r_0	1.19	1.25	1.26	1.18	1.36	1.30	1.09	1.13	1.12	1.19
a_0	0.59	0.52	0.55	0.63	0.74	0.64	0.74	0.69	0.61	0.80
W_v	0	0	0	0	0	0	0	−2.79	4.62	7.99
W_d	12.99	8.03	9.00	15.00	12.97	12.79	8.05	8.68	4.12	9.01
r_w	1.47	1.08	1.06	1.03	1.53	1.57	1.00	1.00	1.42	1.18
a_w	0.19	0.47	0.38	0.29	0.32	0.28	0.71	0.74	0.74	0.57
$V_{\rm sor}$	6.47	7.00	7.00	7.00	7.00	7.00	9.54	9.72	15.02	10.19
$V_{\rm soi}$	2.15	0.10	0.10	0.0	3.94	4.08	0.08	0	0.75	0.13
$r_{\rm so}$	0.93	0.90	0.90	0.98	1.00	1.00	1.15	1.05	0.92	0.90
$a_{\rm so}$	0.35	0.74	0.20	0.20	0.35	0.20	0.70	0.73	0.71	0.56
χ^2	2.4	1.6	1.2	3.9	10.4	9.7	0.2	0.13	1.0	6.7

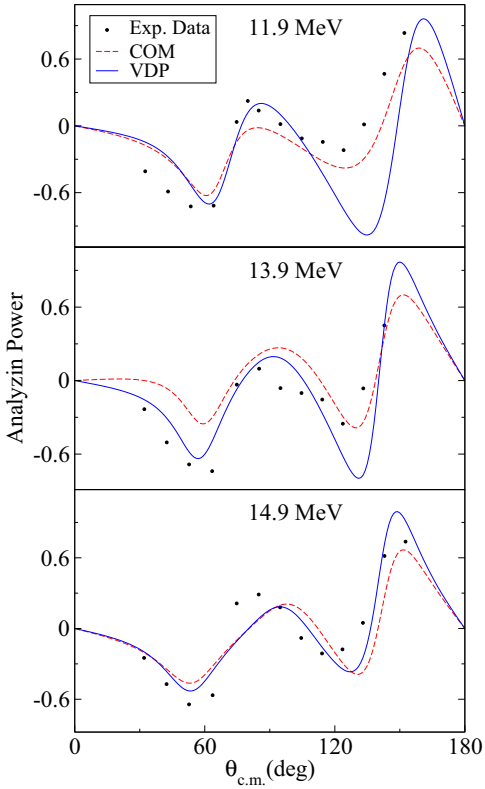

FIG. 5. (Color online) Analyzing power fits for the $n - {}^{12}$C elastic scattering process using the velocity-dependent potential (VDP) and the conventional optical model (COM). The experimental data are obtained from Ref. [28].

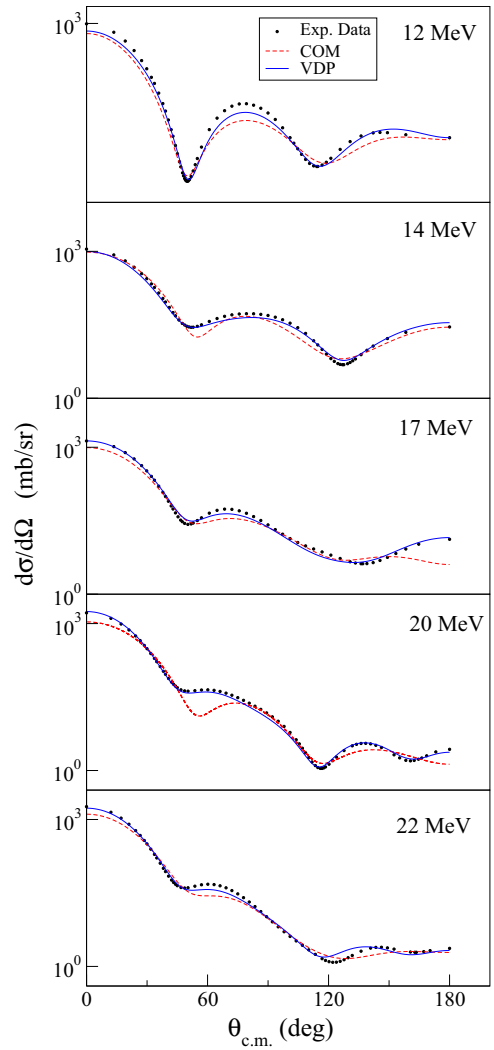

FIG. 6. (Color online) Angular distribution fits for the $n - {}^{16}$O elastic scattering process using the velocity-dependent potential (VDP) and the conventional optical model (COM). The experimental data are obtained from Ref. [32].

predictions for $\sigma_{\text{tot}}^{\text{el}}$ with χ^2 values of almost unity. For the $n - {}^{12}$C scattering process, Table IX shows that the agreement between the theoretical total elastic cross sections obtained using the VDP and COM models is very good with the VDP predictions being more accurate with $\chi^2 = 0.58$. This is also the case for the predicted integrated elastic cross section for the $n - {}^{16}$O scattering process as can be seen in Table X. Regarding the total reaction cross section, the agreement between the theoretical values and the experimental data is less accurate for the the three VDP, DG, and COM models. Clearly, all the three models (DG, VDP, and COM) have resulted in much more accurate predictions for the values of the integrated elastic cross section compared to the total reaction cross-section case. This is not surprising as the parameters of all three models were determined by fitting the elastic angular distribution data. The theoretical predictions for the total elastic cross section in addition to the experimental data are displayed in Fig. 10, where the very good predictions of the VDP are evident particularly in graphs in Figs. 10(b) and 10(c).

V. CONCLUSIONS

Unlike the case for heavy nuclei, the success of the conventional optical model in describing nucleon elastic scattering from the light $1p$-shell nuclei was somewhat limited as we pointed out in the introduction. Light nuclei have surface deformations that result in resonance structures at certain angular and energy ranges [30]. One improvement to the COM would be to include terms that accommodate the effects of surface deformations and nuclear edge diffuseness. A good example is the work in Ref. [17] where the authors added a real surface-peaked term to the optical potential similar to that in [18]. They were able to fit the angular distribution data for elastic neutron scattering from the light ^{9}Be nucleus over the 4- to 136-MeV energy range. The authors interpreted this term as representing the effects of surface deformations which lead to coupling of the ground state to inelastic excitation channels. This is most important in light nuclei which mainly consist of diffused edges. For the $n - {}^9$Be elastic scattering system, the real surface term was also crucial in obtaining the two resonances at the low 0.7- and 3.1-MeV laboratory incident energies. Furthermore, the authors fit the same data using the dispersive optical model (DOM), which contains a real surface term as a consequence of the dispersive relation [16]. Furthermore, a real surface term correction to the

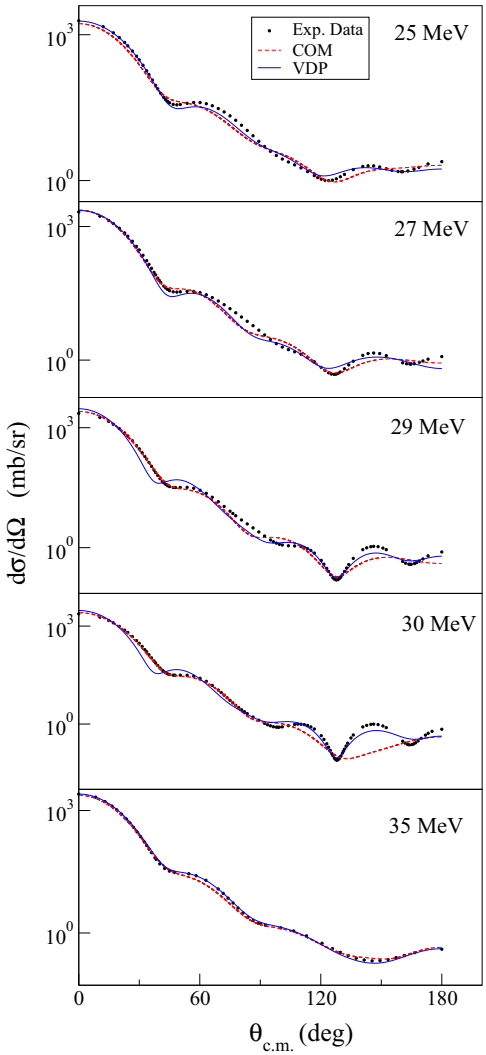

FIG. 7. (Color online) Angular distribution fits for the $n - {}^{16}$O elastic scattering process using the velocity-dependent potential (VDP) and the conventional optical model (COM). The experimental data are obtained from Ref. [32].

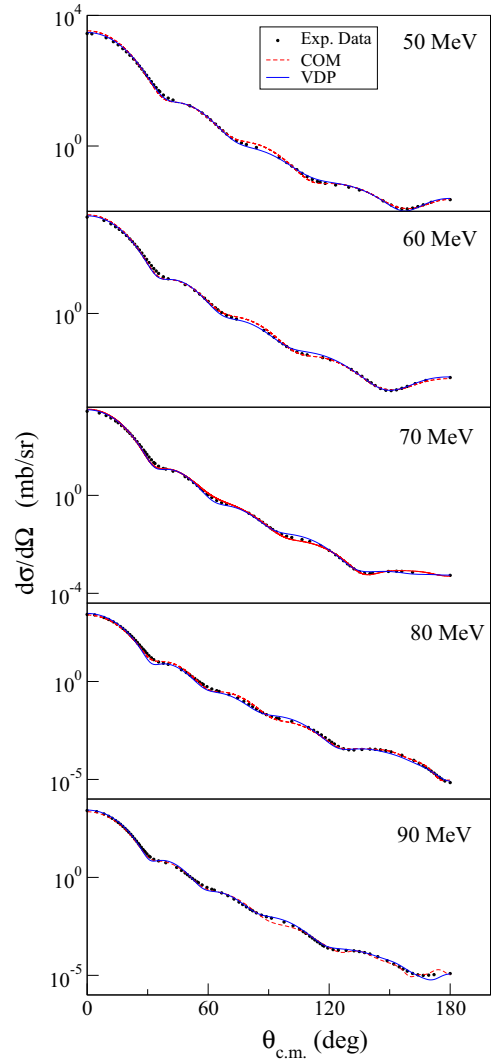

FIG. 8. (Color online) Angular distribution fits for the $n - {}^{16}$O elastic scattering process using the velocity-dependent potential (VDP) and the conventional optical model (COM). The experimental data are obtained from Ref. [32].

smooth Hartree-Fock potential accounted for single-particle states coupling to collective excitations of the nuclear core in $1p$-shell nuclei, and explained the ground states of ^{11}Li, ^{12}Be, and ^{14}C nuclei, which were not possible to describe using the usual COM [18]. In addition, a real surface term correction to the HF potential was obtained from the coupling of single-particle states to the random phase approximation collective one-phonon states of the core [15]. Such vibrational model calculations were successful in explaining the inversion of the $1/2^-, 1/2^+$ states in the one-neutron halo ^{11}Be nucleus.

In this work we have modified the conventional optical model by introducing a real surface term and its higher order derivatives as given in Eq. (9). It is worth noting that one of the resulting surface terms in this work namely $(\rho'(r))^2$ has the same radial form as the term used in [17]. Recently, the VDP was used to describe nucleon elastic scattering from light, medium, and heavy nuclei. It resulted in significant improvements in describing the elastic angular distributions of neutron scattering from the $1p$-shell ^{12}C nucleus [12], the medium ^{40}Ca nucleus [13], and proton elastic scattering from ^{12}C, ^{16}O, ^{54}Fe, and ^{58}Ni [14]. However, the energy ranges considered in the last three references were 12–20 MeV for the neutron case and 12–40 for proton scattering.

In the present work we have investigated the importance of the VDP in describing the light ^{12}C and ^{16}O nuclei by extending the energy range from 12 up to 90 MeV. No lower energies were considered to avoid the region of compound nucleus reactions. For neutron elastic scattering from ^{12}C, we have compared the results of the VDP to those of Dave and Gould [9], who fitted the elastic angular distributions using the COM over the low 7- to 15-MeV energy range. The angular distribution fits are given in Fig. 1. Clearly, the VDP has resulted in significant improvements to the angular distribution fits at large angles for the 12.8-, 14-, and 15-MeV incident energies. At those energies the extra three parameters of $\rho(r)$ in the VDP model are needed to improve the fits, while

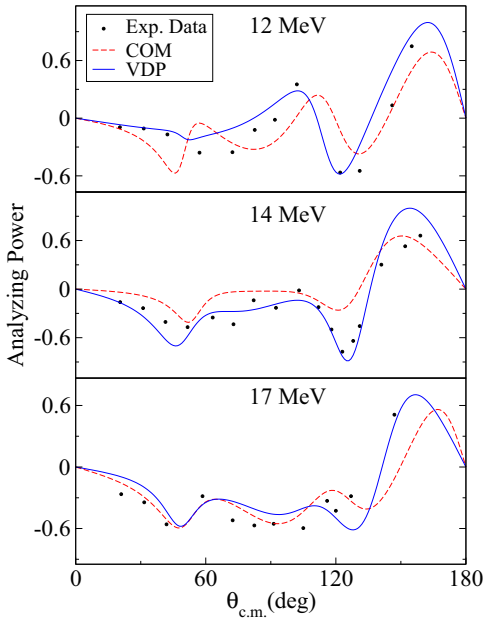

FIG. 9. (Color online) Analyzing power fits for the $n - {}^{16}$O elastic scattering process using the velocity-dependent potential (VDP) and the conventional optical model (COM). The experimental data are obtained from Ref. [28].

they are less important at the lower 9.6 incident energy as both models resulted in an overall similar fits. The presence of the surface terms seem to be important when the differential cross sections show structural effects that are manifested as maxima and minima particularly in the backward-scattering region. In obtaining their fits, Dave and Gould fixed their COM geometrical parameters. Consequently, we have also fixed our geometrical parameters for a meaningful comparison. An exception are the constant values of r_ρ and a_ρ which had to be modified only at 15 MeV, otherwise the corresponding

TABLE V. VDP best fit parameters for $n - {}^{16}$O elastic scattering. Potential depths are in units of MeV, geometric parameters in units of Fermi, and ρ_0 is dimensionless.

VDP	$E_{\rm lab}$ (MeV)					
parameters	35	50	60	70	80	90
V_0	40.0	39.5	39.5	36.7	33.2	32.0
r_0	1.196	1.196	1.196	1.196	1.196	1.196
a_0	0.654	0.654	0.654	0.654	0.661	0.634
W_v	1.0	2.7	7.2	7.2	9.4	12.0
W_d	4.4	4.7	4.7	4.7	4.4	2.7
r_w	1.240	1.240	1.240	1.240	1.240	1.240
a_w	0.670	0.670	0.670	0.670	0.670	0.670
$V_{\rm sor}$	3.5	3.4	3.2	2.9	2.6	2.2
$V_{\rm soi}$	0.0	0.0	0.0	0.0	0.0	0.7
$r_{\rm so}$	1.050	1.050	1.050	1.050	1.040	1.043
$a_{\rm so}$	0.470	0.470	0.470	0.470	0.470	0.470
χ^2	0.7	0.7	1.8	2.4	4.2	3.0

excellent fit at large angles becomes less accurate. The χ^2 values corresponding to the VDP are clearly lower than those of the COM potential as can be seen in Table I.

We have also considered the extended 12- to 90-MeV incident energy range. This time we had to fit the data twice, the first using the VDP while in the other we employed the COM potential. To obtain as good fits as possible we have allowed the potential strengths and geometrical parameters of both models to vary with energy. However, we kept this variation down to a minimum. The results are shown in Figs. 3 and 4. As before, both models lead to similar fits in the forward direction. But the VDP has clearly improved the angular distribution fits in the back-angle scattering region corresponding to certain energies most important of which are 17, 19, and 20 MeV. Above 20 MeV, the differential cross sections do not have structural effects and the COM resulted in excellent fits across the full angular range. Therefore, the surface terms are only

TABLE IV. VDP best fit parameters for $n - {}^{16}$O elastic scattering. Potential depths are in units of MeV, geometric parameters in units of Fermi, and ρ_0 is dimensionless.

VDP	$E_{\rm lab}$(MeV)								
parameters	12	14	17	20	22	25	27	29	30
V_0	51.6	47.5	46.6	41.8	41.8	40.8	40.8	40.5	40.5
r_0	1.188	1.175	1.190	1.195	1.200	1.163	1.150	1.168	1.154
a_0	0.591	0.590	0.598	0.700	0.646	0.608	0.646	0.559	0.556
W_v	0	0	0	0	0	0	0	2.1	2.1
W_d	2.3	4.2	5.4	8.0	8.0	6.7	6.9	8.0	8.6
r_w	1.493	1.240	1.240	1.318	1.240	1.204	1.319	1.448	1.433
a_w	0.661	0.670	0.670	0.503	0.503	0.631	0.670	0.570	0.575
ρ_0	−0.257	−2.175	−0.700	−1.325	−1.070	−1.353	−1.278	−1.515	−1.537
r_ρ	0.957	1.700	1.556	1.533	1.440	1.320	1.320	1.600	1.570
a_ρ	0.150	0.200	0.200	0.219	0.200	0.200	0.200	0.375	0.375
$V_{\rm sor}$	6.6	6.1	3.3	3.1	3.1	2.7	2.4	4.6	4.3
$V_{\rm soi}$	1.0	1.5	3.1	0.0	1.8	1.7	2.8	3.7	3.7
$r_{\rm so}$	1.191	1.050	0.953	1.050	1.050	0.800	1.100	1.100	1.041
$a_{\rm so}$	0.502	0.470	0.470	0.470	0.600	0.600	0.470	0.470	0.450
χ^2	1.8	1.6	2.0	1.0	3.1	2.2	4.9	7.0	8.9

TABLE VI. COM best fit parameters for $n - {}^{16}$O elastic scattering. Potential depths are in units of MeV, geometric parameters in units of Fermi, and ρ_0 is dimensionless.

COM	$E_{\rm lab}$(MeV)								
parameters	12	14	17	20	22	25	27	29	30
V_0	49.86	48.00	48.83	44.49	42.58	40.00	39.00	38.69	38.00
r_0	1.30	1.21	1.23	1.20	1.24	1.34	1.28	1.19	1.27
a_0	0.67	0.57	0.60	0.48	0.60	0.69	0.76	0.86	0.74
W_v	0	0	0	0	0	0	0	0	0.74
W_d	7.00	7.00	11.08	10.76	11.99	9.75	8.38	8.59	7.64
r_w	1.00	1.42	1.02	1.17	1.10	1.20	1.31	1.3	1.32
a_w	0.52	0.39	0.53	0.45	0.43	0.55	0.62	0.55	0.59
$V_{\rm sor}$	8.0	6.0	7.0	9.0	8.0	15.84	12.23	9.86	6.57
$V_{\rm soi}$	1.00	1.16	5.20	0.10	2.43	5.00	4.99	1.40	2.37
$r_{\rm so}$	1.13	0.90	1.00	1.00	0.97	1.08	1.16	1.22	1.05
$a_{\rm so}$	0.74	0.74	0.35	0.74	0.74	0.62	0.74	0.71	0.69
χ^2	5.2	5.0	5.3	7.0	4.5	3.8	3.8	5.8	10.9

needed up to 20-MeV incident neutron energy where structural effects are present. The corresponding best fit parameters are shown in Tables II and III.

The same procedure was followed for the $n - {}^{16}$O elastic scattering process. The angular fits are shown in Figs. 6–8. Clearly, the COM fits deviate from the experimental data around the first minimum ((50°–70°) at the 14- to 20-MeV incident energies. The corresponding VDP fits are clearly more accurate. In the large-angle scattering region the VDP leads to much better fits particularly at the 17- and 30-MeV cases. Above 30 MeV the angular distributions no longer show large-angle deep minima, and hence the COM reproduced the experimental data for the full angular range. Consequently, the surface terms are important up to 30 MeV only, where surface deformation effects seem to be important. The corresponding best fit parameters are shown in Tables IV–VII. Because the VDP is only needed up to 20 MeV for the $n - {}^{12}$C and 30 MeV for the $n - {}^{16}$O elastic scattering processes, we limited the upper limit of our energy range to 90 MeV.

TABLE VII. COM best fit parameters for $n - {}^{16}$O elastic scattering. Potential depths are in units of MeV, geometric parameters in units of Fermi, and ρ_0 is dimensionless.

COM	$E_{\rm lab}$ (MeV)					
parameters	35	50	60	70	80	90
V_0	34.99	32.99	30.94	27.00	23.00	21.00
r_0	1.27	1.30	1.29	1.20	1.21	1.28
a_0	0.71	0.74	0.74	0.68	0.72	0.71
W_v	2.99	3.43	3.04	4.00	6.90	8.00
W_d	7.00	8.00	9.00	8.00	8.02	6.22
r_w	1.13	1.27	1.17	1.41	1.18	1.16
a_w	0.53	0.54	0.63	0.62	0.70	0.68
$V_{\rm sor}$	8.00	6.92	8.36	8.17	14.22	8.45
$V_{\rm soi}$	0	−3.67	−2.85	−4.91	−0.46	−0.42
$r_{\rm so}$	0.90	1.05	0.98	1.20	0.90	0.90
$a_{\rm so}$	0.75	0.52	0.66	0.51	0.72	0.68
χ^2	1.1	1.3	1.4	1.9	2.7	3.3

By inspecting the best fit parameters in Tables II–VII, one observes that in each of the carbon and oxygen cases the parameters of the VDP and COM formalisms have similar energy variations apart form the strength W_d of the imaginary surface absorption term. In each case the values of W_d corresponding to the VDP are reduced compared to the corresponding values of COM. This could be a consequence of the real surface terms $\rho(r)$ and its higher derivatives given in Eq. (9) accounting, at least partly, for the effects of the nuclear surface deformations. Such deformations play an important role in coupling the ground state of the target nucleus to inelastic excitations, thus modifying the elastic angular distribution data.

In all the cases considered above, we have compared the analyzing powers calculated using the VDP and COM formalism. The plots are shown in Figs. 2, 5, and 9. The analyzing powers calculated using the VDP and COM lead to reasonable descriptions of the experimental polarization data. However, the VDP was found to be more accurate in describing the data at small angles. At large angles, however, the analyzing power values of both models are less accurate with the COM values being closer to the experimental data at some specific incident energies.

TABLE VIII. Total elastic and reaction cross sections using the VDP and DG models corresponding to the $n - {}^{12}$C elastic scattering process. The experimental values are obtained from Ref. [31].

$E_{\rm lab}$ (MeV)	Total elastic cross section (mb)			Total reaction cross section (mb)		
	Experimental	VDP	DG	Experimental	VDP	DG
9.6	691.0	609.1	665.4	538.3	413.9	445.0
11.0	901.3	733.0	730.5	522.6	413.9	428.5
12.8	904.4	802.5	805.1	473.8	371.1	418.3
14.0	803.3	847.1	848.7	499.8	371.1	414.3
15.0	851.4	814.5	880.8	550.3	424.2	411.0
χ^2		1.3	1.1		5.2	3.4

TABLE IX. Total elastic and reaction cross sections using the VDP and COM models corresponding to the $n - {}^{12}$C elastic scattering process. The experimental values are obtained from Ref. [31].

E_{lab} (MeV)	Total elastic cross section (mb)			Total reaction cross section (mb)		
	Experimental	VDP	COM	Experimental	VDP	COM
12	927.6	751.5	799.2	525.1	595.2	542.8
14	803.3	738.9	718.8	499.8	601.8	587.1
15	851.4	857.1	776.2	550.3	617.6	553.4
17	842.9	885.4	752.5	549.0	615.2	536.2
19	957.8	985.0	882.2	529.2	691.0	748.3
20	1008.9	969.5	914.4	522.7	620.1	634.7
22	905.2	923.1	854.8	501.5	614.6	672.5
30	891.4	901.8	856.1	412.3	545.2	561.8
50	640.2	699.1	549.0	309.6	504.7	530.7
80	367.5	380.2	358.4	250.8	375.2	442.2
χ^2		0.58	0.90		10.2	15.9

In Table VIII we compare the total elastic and reaction cross sections calculated using the VDP and Dave and Gould models to the experimental results. Judging by the $\chi^2 \approx 1$ values, both models have resulted in very good predictions for the integrated elastic cross section. For the $n - {}^{12}$C and $n - {}^{16}$O scattering processes Tables IX and X show the VDP and COM theoretical predictions for the total elastic cross section in addition to the experimental data. The χ^2 values show that both the VDP and COM models result in very good predictions for the total elastic cross section with the VDP predicting more accurate values particularly for the ^{16}O case especially at low energies where the surface terms are important. For all three models the theoretical predictions for the total reaction

TABLE X. Total elastic and reaction cross sections using the VDP and COM models corresponding to the $n - {}^{16}$O elastic scattering process. The experimental values are obtained from Ref. [31].

E_{lab} (MeV)	Total elastic cross section (mb)			Total reaction cross section (mb)		
	Experimental	VDP	COM	Experimental	VDP	COM
12	1036.8	873.9	752.9	611.9	632.6	759.8
14	946.3	844.5	888.4	635.5	767.6	676.6
17	1005.3	957.4	821.5	601.6	739.3	714.1
20	998.7	999.3	780.8	640.3	795.9	625.7
22	1046.5	991.1	844.8	622.5	692.1	625.0
25	1017.6	973.8	845.0	612.0	695.4	722.3
27	1023.1	994.4	989.4	583.0	769.0	782.4
29	1032.9	1027.3	1044.6	537.0	905.6	709.5
30	1042.8	998.0	1033.0	524.1	910.9	717.4
35	1012.9	1039.7	948.8	467.0	527.6	537.4
50	809.8	862.9	910.8	390.1	513.1	549.2
60	663.1	709.9	748.9	370.0	559.6	559.0
70	578.1	625.3	646.1	336.7	530.2	602.6
80	485.3	516.4	452.5	321.9	524.1	567.3
90	404.2	447.2	368.2	300.0	465.4	487.8
χ^2		0.52	1.93		18.0	16.9

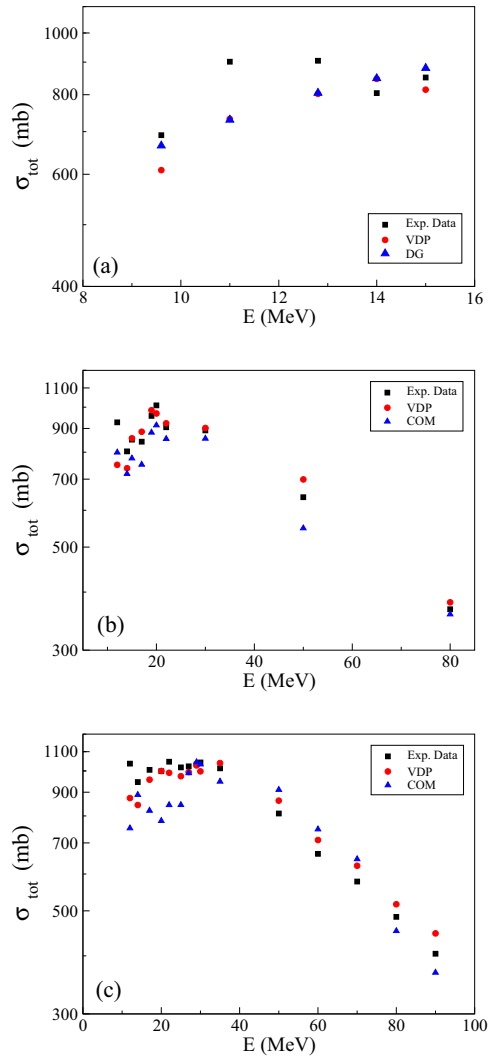

FIG. 10. (Color online) Total elastic cross section calculated using the DG, VDP, and COM models compared to the experimental data which is obtained from Ref. [31]. Graphs (a) and (b) correspond to the $n - {}^{12}$C elastic scattering process, while graph (c) is for the $n - {}^{16}$O elastic scattering process.

cross section are less accurate compared to the corresponding total elastic cross-section case. This is not surprising as the parameters of each potential were determined by fitting the elastic angular distribution data. In Fig. 10 we display the integrated elastic cross sections for the three models together with the experimental data.

In summary, the VDP has resulted in significant improvement in fitting the elastic $n - {}^{12}$C and $n - {}^{16}$O angular distributions particularly in the back-angle scattering region corresponding to certain energy ranges. It is worth noting that several earlier works that we discussed in the introduction have reported difficulties in fitting the elastic angular distribution data corresponding to nucleon scattering from light 1-p shell nuclei, particularly in the back-angle region. The VDP has also resulted in very good theoretical predictions for the integrated elastic cross section in addition to good predictions for the analyzing power $A_y(\theta)$. We propose that the real surface terms

$\rho(r)$ and its higher derivatives are important in accounting for the effects of surface deformations and edge diffuseness in light nuclei, and might simulate coupling of the ground state to inelastic excitation channels. This conclusion is in line with the results of other works that introduced a real surface term in the optical model which were discussed in the introduction.

Finally, coupling of the elastic channel to inelastic excitations is simulated by the imaginary part of the optical potential and leads to a loss of particle flux into the open reaction channels. In the Feschbach formalism, such couplings also result in a second-order complex potential term. The real part of this second-order term is called a polarization potential and renormalizes the *bare* real part of the optical potential [33] and [34]. This polarization potential arises whenever coupled-channel calculations are reduced to a one-channel problem. Consequently, the hypothesis that the real surface terms introduced by the VDP simulate coupling of the elastic channel to inelastic excitations imply that they represent a polarization potential. One may test this hypothesis by investigating the effect of a complex $\rho(r)$ term on the VDP angular distribution fits and theoretical integrated cross section predictions. If $\rho(r)$ represents a polarization potential, then the imaginary part of $\rho(r)$ would add to the second-order complex term, while its real part represents the polarization potential. An improvement in the model's predictions would support the claim that the current real surface terms represent a polarization potential and, therefore, simulate coupling to open reaction channels. If no improvement in the model's predictions is obtained, the origin of the real surface terms may be from a change in the real part of the nucleon-nucleus potential inside the nuclear medium and hence might simulate effects that are represented by real potentials such as, for example, exchange or knock-on effects. Obviously, further investigations are needed to shed more light on the physical origin of the real surface terms introduced by the VDP.

[1] P. E. Hodgson, *Nuclear Reactions and Nuclear Structure* (Clarendon, Oxford, 1971).
[2] A. J. Koning and J. P. Delaroche, Nucl. Phys. A **713**, 231 (2003).
[3] J. Klug, J. Blomgren, A. Atac, B. Bergenwall, A. Hildebrand, C. Johansson, P. Mermod, L. Nilsson, S. Pomp, U. Tippawan, K. Elmgren, N. Olsson, O. Jonsson, A. V. Prokofiev, P. U. Renberg, P. Nadel-Turonski, S. Dangtip, P. Phansuke, M. Osterlund, C. LeBrun *et al.*, Phys. Rev. C **68**, 064605 (2003).
[4] R. Kozack and D. G. Madland, Nucl. Phys. A **509**, 664 (1990).
[5] P. Romain and J. P. Delaroche, in *Proceedings of a Specialists Meeting*, edited by P. Nagel (OECD, Paris, 1997), p. 167; see http://db.nea.fr/html/science/om200/.
[6] K. Amos, P. J. Dortmans, H. V. von Geramb, S. Karataglidis, and J. Raynal, Adv. Nucl. Phys. **25**, 275 (2000).
[7] E. Bauge, J. P. Delaroche, and M. Girod, Phys. Rev. C **63**, 024607 (2001).
[8] R. Crespo, R. C. Johnson, and J. A. Tostevin, Phys. Rev. C **46**, 279 (1992).
[9] J. H. Dave and C. R. Gould, Phys. Rev. C **28**, 2212 (1983).
[10] B. A. Watson, P. P. Singh, and R. E. Segei, Phys. Rev. **182**, 977 (1969).
[11] G. H. Rawitscher and D. Lukaszek, Phys. Rev. C **69**, 044608 (2004).
[12] M. I. Jaghoub, M. F. Hassan, and G. H. Rawitscher, Phys. Rev. C **84**, 034618 (2011).
[13] M. I. Jaghoub, Phys. Rev. C **85**, 024606 (2012).
[14] R. A. Zureikat and M. I. Jaghoub, Nucl. Phys. A **916**, 183 (2013).
[15] N. Vinh Mau, Nucl. Phys. A **592**, 33 (1995).
[16] C. Mahaux and R. Sartor, Adv. Nucl. Phys. **20**, 1 (1991).
[17] A. Bonaccorso and R. J. Charity, Phys. Rev. C **89**, 024619 (2014).
[18] N. Vinh Mau and J. C. Pacheco, Nucl. Phys. A **607**, 163 (1996).
[19] G. R. Satchler and W. G. Love, Phys. Rep. **55**, 183 (1979).
[20] C. H. Johnson, D. J. Horen, and C. Mahaux, Phys. Rev. C **36**, 2252 (1987).
[21] L. S. Kisslinger, Phys. Rev. **98**, 761 (1955).
[22] H. Feshbach, Ann. Phys. **5**, 357 (1958).
[23] M. I. Jaghoub, Eur. Phys. J. A **27**, 99 (2006).
[24] M. I. Jaghoub, Phys. Rev. A **74**, 032702 (2006).
[25] M. Krell and T. E. O. Ericson, Nucl. Phys. B **11**, 521 (1969).
[26] F. G. Perey, Phys. Rev. **131**, 745 (1963).
[27] X. Li and L. Chen, Nucl. Phys. A **874**, 62 (2012).
[28] EXFOR: Experimental Nuclear Reaction Data, https://www-nds.iaea.org/exfor/exfor.htm.
[29] H. V. Geramb and K. Amos, Phys. Rev. C **12**, 1697 (1975).
[30] H. V. Geramb, Nucl. Phys. A **183**, 582 (1972); H. V. Geramb, R. Sprickmarn, and G. L. Strobel, *ibid.* **199**, 545 (1973); K. A. Amos and R. Smith, *ibid.* **226**, 519 (1974).
[31] ENDF: Evaluated Nuclear Data File, Library: JENDL/HE-2007.
[32] ENDF: Evaluated Nuclear Data File, B-VII.1.
[33] I. J. Thompson and F. M. Nunes, *Nuclear Reactions for Astrophysics* (Cambridge University Press, Cambridge, 2009).
[34] C. H. Dasso, S. Landowne, G. Pollarolo, and A. Winther, Nucl. Phys. A **459**, 134 (1986).